ELSEVIER

Ultramicroscopy 69 (1997) 39–49

ultramicroscopy

Surface potential mapping: A qualitative material contrast in SPM

H.O. Jacobs, H.F. Knapp, S. Müller, A. Stemmer*

Nanotechnology Group, Institute of Robotics, ETH Center/CLA, CH-8092 Zurich, Switzerland

Received 2 January 1997; received in revised form 11 March 1997

Abstract

Electric potential measurements on different metals and semiconductors have been performed using a scanning probe microscope. The measured potential shows a clear chemical contrast in all cases, allowing us to differentiate between different materials down to 100 nm in size with potential noise smaller than 1 mV. The lateral potential resolution as a function of the tip–sample distance has been measured and numerical calculations of the force density acting on the tip are presented along with theoretical examinations of the quantitative potential resolution.

Keywords: Surface potential; Contact potential; Kelvin probe; SPM; AFM; Chemical contrast

1. Introduction

In semiconductor devices and biological samples, the local electric potential distribution is of significant interest and provides us with a better description and understanding of the specimen's composition and function. Several researchers developed techniques to use a scanning tunneling microscope (STM) to measure the local potential distribution on material surfaces [1–5]. These techniques show a resolution on the nanometer scale but are limited to conductive samples requiring a tunneling current for operation. The first surface potential measurements using an atomic force microscope (AFM) were performed by Martin et al. [6, 7]. Subsequently, Weaver and Abraham introduced the modulation method [8] and Nonnenmacher et al. applied the Kelvin probe force microscope (KFM) to measure the surface potential between different metals [9, 10]. Since then, various improvements on the basic method have been made [11–13].

In most current set-ups, the tip is vibrating in non-contact mode above the surface at two different frequencies. Topography and potential can then be measured simultaneously. However, lateral resolution of the topographic image is influenced by long-range electrostatic forces [12].

Therefore, in our set-up, topography and potential are measured sequentially with minimal cross talk using the lift-mode technique implemented in our commercial AFM.

* Corresponding author.

PII S0304-3991(97)00027-2

2. Theory of material contrast in KFM

Electrons in different materials have different chemical binding energy. When two different materials are electrically connected, electrons flow from the material with the smaller work function Φ_{m2} (weak binding) to the material with the higher work function Φ_{m1} (strong binding; Fig. 1a). This diffusion current builds up a double layer at the interface resulting in an electrostatic potential difference $\Delta\Phi$ (contact potential) between the two materials. This potential difference at the interface shifts the bulk electron energy levels until the Fermi levels W_f of the two materials are matched. When this equilibrium is reached, the electrostatic force cancels the diffusion force in the interface and the contact potential equals the difference of the two work functions (Fig. 1b).

Outside of the bulk materials the now different surface potentials cause electrostatic forces between the surfaces. This attractive force is given by

$$F_z = \frac{1}{2}\frac{dC}{dz}(\Delta\Phi)^2, \tag{1}$$

where C is the capacitance and $\Delta\Phi$ the contact potential between the two materials, i.e. tip and specimen.

Generally, KFM uses this resulting electrostatic force as a signal to adjust an external voltage to compensate the contact potential until the force vanishes. This is achieved when the external voltage is equal to the difference of the two work functions (Fig. 1c). When the specimen consists of different materials, each material interface has its specific contact potential causing a local variation of the surface potential (Fig. 1d) which can now be mapped by locally adjusting the external voltage U to zero the electrostatic force.

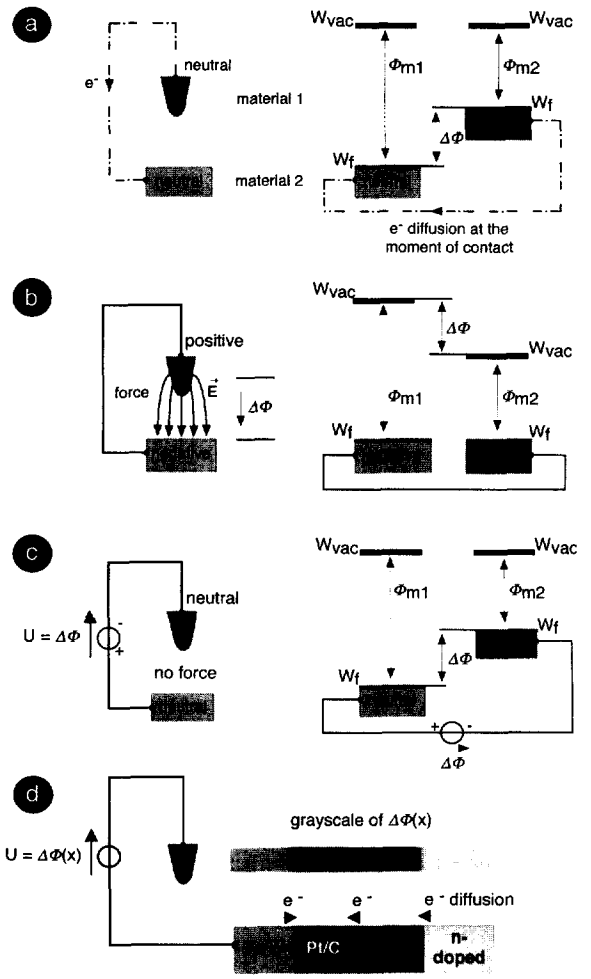

Fig. 1. Energy diagrams of sample and conducting tip: (a) Neutral tip and sample before being electrically connected. (b) Interaction force and electrostatic potential difference after electron diffusion. (c) External potential applied to zero the force. (d) Gray-scale representation of the potential compensating the local force on different materials. Darker regions represent a lower ('negative'), brighter regions a higher ('positive') value of surface potential (W_{vac}: vacuum energy level, W_f: Fermi energy, ϕ_{mi}: work function of material i, $\Delta\phi$: work function difference between material 1 and 2).

3. Materials and methods

3.1. Simulation of electrostatic tip–sample interaction

As the measurement of the surface potential depends on long-range electrostatic interactions between tip and sample, the resolution of this method not only depends on the tip's apex but also on the tip's side walls, albeit to a lesser extent. To get information about the total acting force, the local force density, and resolution one has to solve

Maxwell's equations. However, analytical solutions for the tip–sample interactions can only be found for very simple geometrical configurations like a conducting sphere over a flat conducting sample. Therefore, in our approach we used a simulation tool (multiple multipole method, MMP) recently developed to analyze electromagnetic fields in near-field optics [14] which is also capable of solving electrostatic problems [15].

The AFM tip was approximated to be conducting and rotationally symmetric. Tip length 15 μm, total opening angle 36°, and tip radius 10 nm were chosen to suit the specifications of the commercially available tapping-mode cantilevers used in our experiments.

3.2. Experimental details

All measurements were made at ambient pressure with a commercial AFM (NanoScope® IIIa MultiMode™ with Extender™ Electronics Module, Digital Instruments). Topography was imaged in TappingMode™,whereas potential was imaged using the built-in LiftMode™ feature.

3.2.1. Potential imaging

Since the electrostatic force interaction due to the different surface potentials described above is weak, a frequency sensitive feedback was used to measure the local surface potential (Fig. 2a). To this end, an AC voltage with adjustable DC offset was applied to the conducting AFM-tip. The electrostatic force interaction between the two electrodes (Eq. (1)) then becomes

$$F_z = \frac{1}{2}\frac{dC}{dz}(\Delta\Phi(x) - U_{DC} - U_{AC}\sin(\omega t))^2 \qquad (2)$$

with spectral components at DC

$$F_{DC} = \frac{1}{2}\frac{dC}{dz}\left((\Delta\Phi(x) - U_{DC})^2 + \frac{U_{AC}^2}{2}\right) \qquad (3)$$

and at frequencies ω and 2ω

$$F_\omega = -\frac{dC}{dz}((\Delta\Phi(x) - U_{DC})\,U_{AC}) \qquad (4)$$

$$F_{2\omega} = -\frac{1}{4}\frac{dC}{dz}U_{AC}^2. \qquad (5)$$

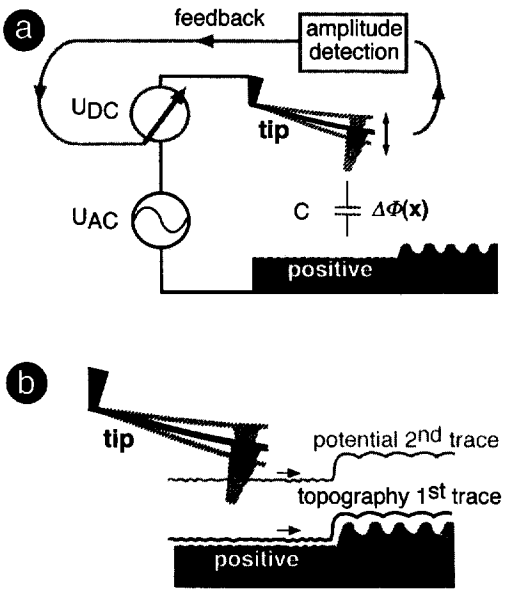

Fig. 2. Kelvin probe method in lift mode: (a) Principle of measuring the local surface potential with an AC-modulated feedback. (b) Measurement cycle: Topography is scanned in a first trace and immediately retraced at a set distance from the surface (lift height) while using the AC-modulated feedback to measure the surface potential.

Using the ω-component of F_z as our feedback signal, the oscillation amplitude of the cantilever was zeroed by adjusting the external DC voltage U_{DC} until it matched $\Delta\Phi(x)$. Maximum sensitivity is achieved when the AC voltage applied to the tip has the resonance frequency of the cantilever.

To obtain a potential image, the specimen was first scanned in tapping mode to determine the surface topography. During this scan no external voltage was applied to the tip to keep long-range electrostatic interactions small. Using the built-in lift-mode feature of our AFM, each acquired scan line was immediately retraced at a set lift height from the sample while the feedback described above was activated (Fig. 2b). The compensating voltage U_{DC} representing the local surface potential was sampled with the same pixel density as topography. The AC voltage applied between tip and sample was 10 Vpp and tuned to the first resonance frequency of the cantilever. The scan frequency was 1 Hz, i.e. the acquisition time for a 256^2 pixel image was 8 min.

It is important to choose a lift height where the cantilever can oscillate freely during the lift cycle. Otherwise topographic features will contribute to the surface potential image. Usually, a 10 nm lift height is sufficient to prevent topographic cross talk.

3.2.2. Tip preparation and electrical connections

To obtain conducting probes, standard tapping-mode silicon cantilevers (f_r = 200–400 kHz, C = 20–100 N/m, R_{tip} = 5–10 nm, cone angle 36°) were first glow-discharged for 10 s and then rotary-shadowed with 6 nm Pt–C at an elevation angle of 45°. Inspection of the probes by scanning electron microscopy (Hitachi S-900) revealed that in most cases a continuous metal film covered the tips' apex (data not shown). Tips can be used for several scans until potential imaging becomes unstable. SEM images of these tips show that either the Pt–C film is removed from the tips' apex or the tips have been contaminated by small particles.

To allow potential control of the cantilever independent of the microscope body (and cantilever holder), we modified the standard all-metal tapping-mode cantilever holder by electrically insulating the leaf spring, holding the cantilever against the piezo, with a Teflon washer and a nylon screw. A thin wire was then soldered to the leaf spring and connected to a contact pin on the holder leading to the AC/DC voltage source (Extender module in our case).

3.2.3. Composite Pt–C/Ta–W substrates

We extended a published protocol [16] to prepare Pt–C islands on Ta–W films and vice versa (Fig. 3). In both cases the metal film on the glass substrate was masked with NaCl crystals before the second 5 nm thick metal film was evaporated onto the surface. Rinsing with ultrapure water dissolved the salt crystals and resulted in the desired structure.

3.2.4. GaAs-FET transistor as active device

As a second test structure, a GaAs-FET transistor was mounted on a flat ceramic substrate and electrically connected with its contact pads by wire bonding. Two external voltage sources were then connected to the device to control drain-source U_{ds} and gate-source voltage U_{gs}. Images of the surface potential of the whole transistor surface under different biasing conditions were taken.

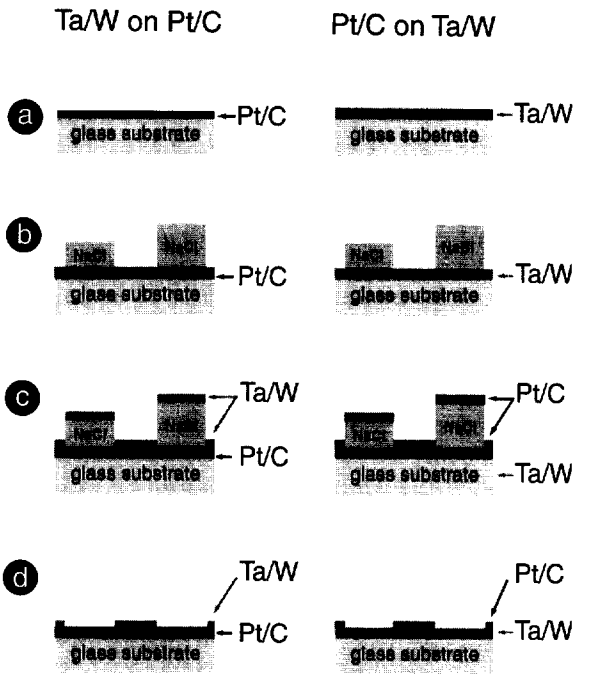

Fig. 3. Basic processing steps to fabricate Ta–W on Pt–C and Pt–C on Ta–W structures. First, a 30% saturated NaCl solution is spread on the metal film, initially evaporated onto a glass substrate. After drying in a stream of N_2, NaCl crystals are scattered across the surface. Next, the second metal film is evaporated on the surface at 90° incidence. Rinsing with ultrapure water removes the NaCl crystals including their metal caps and leaves the desired structure.

3.2.5. Cleaved surface of a vertical cavity laser

This stack of epitaxially grown AlGaAs/AlAs layers formed two distributed Bragg reflectors, one in a p-doped and the other one in a n-doped region. Each reflector by itself consisted of a stack of $Al_{0.15}Ga_{0.85}As$ and AlAs layers, 65 nm and 75 nm thick, respectively. For measurements the cleaved wafer stack was mounted on a metal substrate.

4. Theoretical results

4.1. Simulation of the electrostatic force interaction

Fig. 4a and Fig. 4b show the electrostatic field around the tip for a 15 nm tip–sample separation.

The contours of constant electric field intensity $|E|^2$ decrease by a factor of 4 for successive lines. From Fig. 4c, displaying the force acting on the tip within a radius x_{int}, we conclude that the interaction is concentrated at the tip's apex. To obtain a more quantitative measure of this confinement, we calculated, for different lift heights, the tip area on which 50% of the total force acts. x_{50}, the x coordinate of the border of this area, is plotted versus the tip–sample separation h in Fig. 4d. Thus, for tip–sample separations below 20 nm, 50% of the tip force acts on the tip within a border of 100 nm. x_{50} was calculated from the total attractive electrostatic force, normalized to 1 V potential difference between tip and sample (Fig. 4e). The latter curve demonstrates that the available signal for the feedback decreases rapidly when the tip–sample separation is increased. The two electrode case, i.e. the simulation of the force interaction between a conducting tip with potential Φ_t and a conducting surface with potential Φ_1, shows that for the given tip geometry the force interaction is concentrated around the tip's apex. The two electrode simulation can thus be used to test the effect of altered tip geometries, it does not, however, answer the question of accuracy and resolution of the method.

4.2. Relation between measured potential and true surface potential distribution

To address the question of accuracy and resolution of potential measurements, we consider two regions with constant surface potentials Φ_1 and Φ_2, respectively, and the tip with potential Φ_t (Fig. 4f). The attractive electrostatic force between tip and sample (Eq. (1)) can now be extended to

$$F_z = \tfrac{1}{2} C'_{1t} (\Phi_1 - \Phi_t)^2 + \tfrac{1}{2} C'_{2t} (\Phi_2 - \Phi_t)^2, \tag{6}$$

where the first force component is related to area 1 and the second to area 2. C'_{1t} and C'_{2t} represent derivatives of the capacitance ($\partial C/dz$) and depend on the lateral tip location.

Setting, $\Phi_t = U_{DC} + U_{AC} \sin(\omega t)$, Eq. (4) becomes

$$F_\omega = - C'_{1t} (\Phi_1 - U_{DC}) U_{AC} - C'_{2t} (\Phi_2 - U_{DC}) U_{AC}. \tag{7}$$

The DC tip potential to zero F_ω is given by

$$U_{DC} = \frac{C'_{1t}\Phi_1 + C'_{2t}\Phi_2}{C'_{1t} + C'_{2t}}. \tag{8}$$

For N areas with different surface potentials Φ_i, the measured potential is described by

$$U_{DC} = \frac{\sum_i C'_{it}\Phi_i}{\sum_i C'_{it}}. \tag{9}$$

To obtain a better understanding of Eq. (8), we consider a sample consisting of an area 1 with arbitrary potential Φ_1 surrounded by an area 2 with $\Phi_2 = 0$ V. The measured potential depending on the lateral tip location then becomes

$$U_{DC} = \frac{C'_{1t}}{C'_{1t} + C'_{2t}} \Phi_1. \tag{10}$$

We now see that for tip locations just above the center of area 1 the measured potential will be close to Φ_1 as C'_{1t} is at its maximum and C'_{2t} is at its minimum. Moving away from this point decreases C'_{1t} and increases C'_{2t} so that the measured potential U_{DC} gets smaller.

The above considerations show that resolution and accuracy are defined by the capacitances between the tip and the respective surface regions. Thus, we are led to the following consequences. First, an ideal potential step on a surface will be measured as a smoothed step potential. Second, the measured potential of an area will approach the value of the surrounding surface potential as the area decreases in size. For example, the MMP simulation for an area of radius 10 nm with potential Φ_1, surrounded by an infinitely large area of 0 V showed that only 2% of Φ_1 can be measured with the given tip geometry at 15 nm lift height. Third, the generalized Eq. (9) states that the measured potential (U_{DC}) actually is a weighted average over all potentials Φ_i on the surface, the derivatives of the capacitances C'_{it} being the weighting factors.

5. Experimental results

5.1. Accuracy of the feedback electronics

To measure the noise values and the accuracy of the measured potential, we applied a square-wave

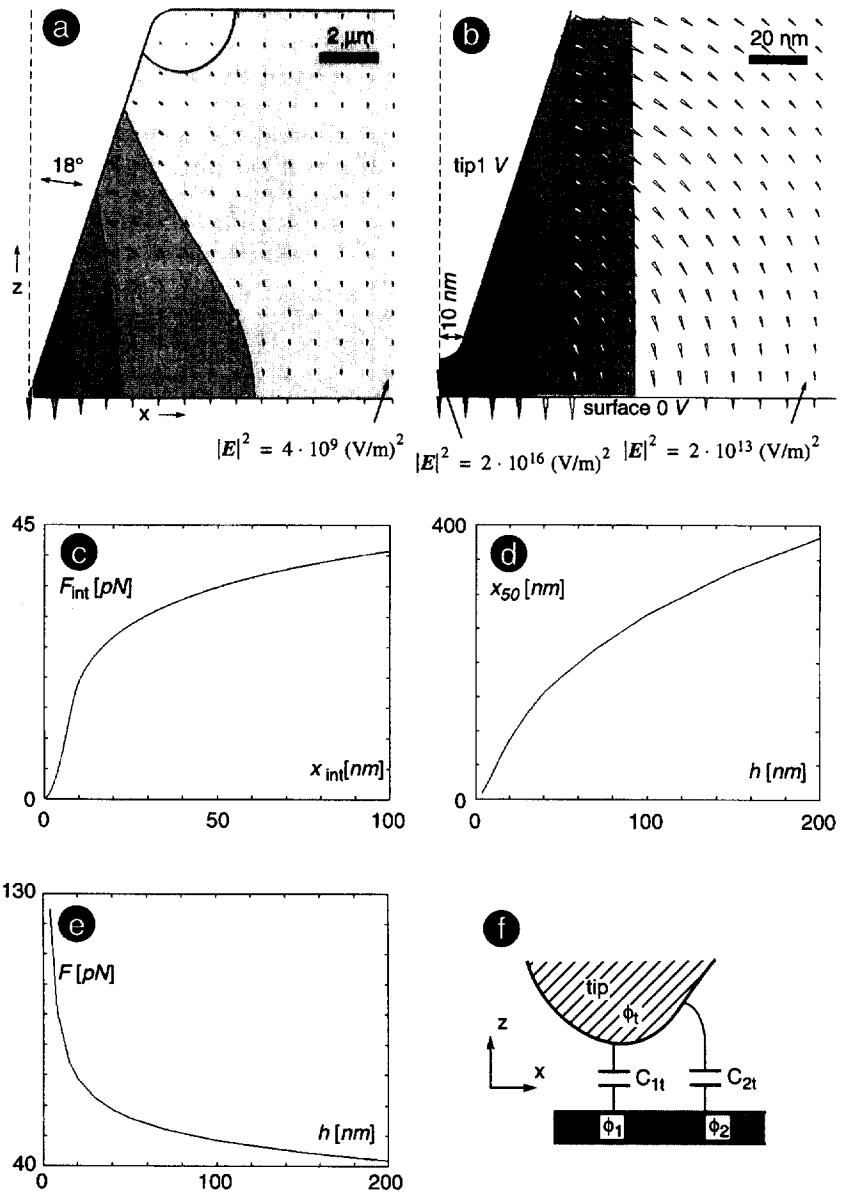

Fig. 4. MMP simulation of electrostatic field and force acting on a conducting cantilever. Tip length, opening angle and apex radius were chosen to suit the specifications of the cantilevers used in our experiments. (a)–(c) were calculated for 15 nm lift height. Overview (a) and close-up (b) show contour lines of constant electric field intensity $|E|^2$ between tip and sample (factor of 4 between successive contour lines, total range in (a): ~ 6 orders of magnitude). Arrows represent the local electric field vectors in strength and direction. (c) z-component of the force portion F_{int} acting on the tip surface within an area of radius x_{int} (calculated by integrating the force acting on the tip surface from $x = 0$ to x_{int}). (d) Value of x_{int} for 50% of the total electrostatic force interaction plotted as a function of lift height h. (e) Total force interaction F as a function of the lift height h (calculated by integrating the force acting on the tip from $x = 0$ to 15 µm). (f) Schematic of the three electrode model used to derive the relation between measured potential and surface feature size.

voltage (4 mVpp, 20 Hz) to a conducting gold substrate (template stripped gold; [17]) and measured the surface potential at a lift height of 20 nm without scanning the surface. The measured potential (Fig. 5) shows that potential steps < 4 mV can be detected with potential noise < 1 mV.

5.2. *Pt–C/Ta–W substrates*

Ta–W always appears positive by ~ 300 mV versus Pt–C in the potential images, independent of its location, i.e. top or bottom layer (Fig. 6). Thus, with this material contrast we can clearly distinguish between areas of different chemical composition. Furthermore, surface features down to several tens of nanometers in size can be detected in the potential image (white arrows in Fig. 6d and Fig. 6e). In addition to the Pt–C and Ta–W layers, other materials can be detected in the potential image Fig. 6e (black arrow) which are also visible in the topography image Fig. 6d as 5 nm thick patches. That these features are not due to topography cross talk can be seen in the backscattered electron SEM image (Fig. 6b), where they show a material contrast different from the Pt–C and Ta–W layers. These patches are the former metal film caps of the salt crystals, which fold onto the surrounding metal film during the rinsing cycle leaving the sides previously in contact with the salt crystals exposed towards the tip.

To investigate the influence of lift height on resolution, potential profiles along the three lines indicated in Fig. 6e were taken for different lift heights. The distance between 25% and 75% of the total measured potential difference Δl_{50} is plotted against lift height in Fig. 7. The graph shows that if the lift height is increased from 2 to 250 nm the length Δl_{50} increases by 200 nm. We conclude that the lift heights used in our experiments (10–15 nm) do not appreciably deteriorate the resolution of the potential image but provide us with a safety margin, since at too low lift heights the tip might accidentally touch the surface inducing topographic features in the potential image.

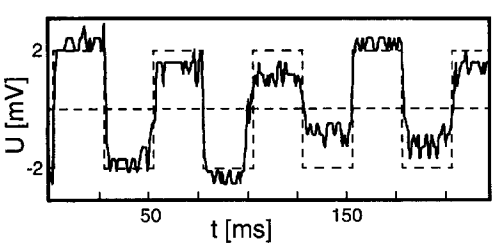

Fig. 5. Accuracy of the measured surface potential. The measured surface potential (solid line) follows the external voltage (dashed line) applied to the template stripped gold substrate.

5.3. *GaAs-FET transistor as active device*

Fig. 8a and Fig. 8b show topography and surface potential when no external voltage is applied to the transistor. GaAs forms the bottom layer of the device whereas all higher layers are coated with a 180 nm thick Au-layer, which forms contact pads to drain, source, and gate. In the surface potential image the GaAs surface has a 250 mV higher potential than the Au-coated FET electrodes, which is in good agreement with the 300 mV difference in work function of the materials ($W_{\mathrm{vac,Au}} = 5.1$ eV, $W_{\mathrm{vac,GaAs}} \approx 4.8$ eV [18, 19]).

When an external voltage is applied to the transistor, the energy bands bend and the local surface potential is changed. The surface potential of the active transistor is imaged in Fig. 8c and Fig. 8d for negative and positive bias, respectively. For an applied bias of 1 V, the measured potential difference between drain and source was -0.92 V for negative and 0.90 V for positive bias. The actual error is smaller than 10% because the transistor was protected against damage by using a current limiting voltage source.

5.4. *Cleaved surface of a vertical cavity laser*

In the topography image (Fig. 9a) a modulation in height of approximately 8 nm can be seen between the AlAs and the $Al_{0.15}Ga_{0.85}As$ layers, which is explained by the stronger tendency of AlAs to oxidize and, thereby, grow outward faster [20]. The potential image (Fig. 9b) reveals a clear contrast of 150 mV between the n-doped and p-doped region, which cannot be seen in the topography image. In the n-doped region, donors are left positive after giving off an electron whereas in the p-doped region acceptors are left

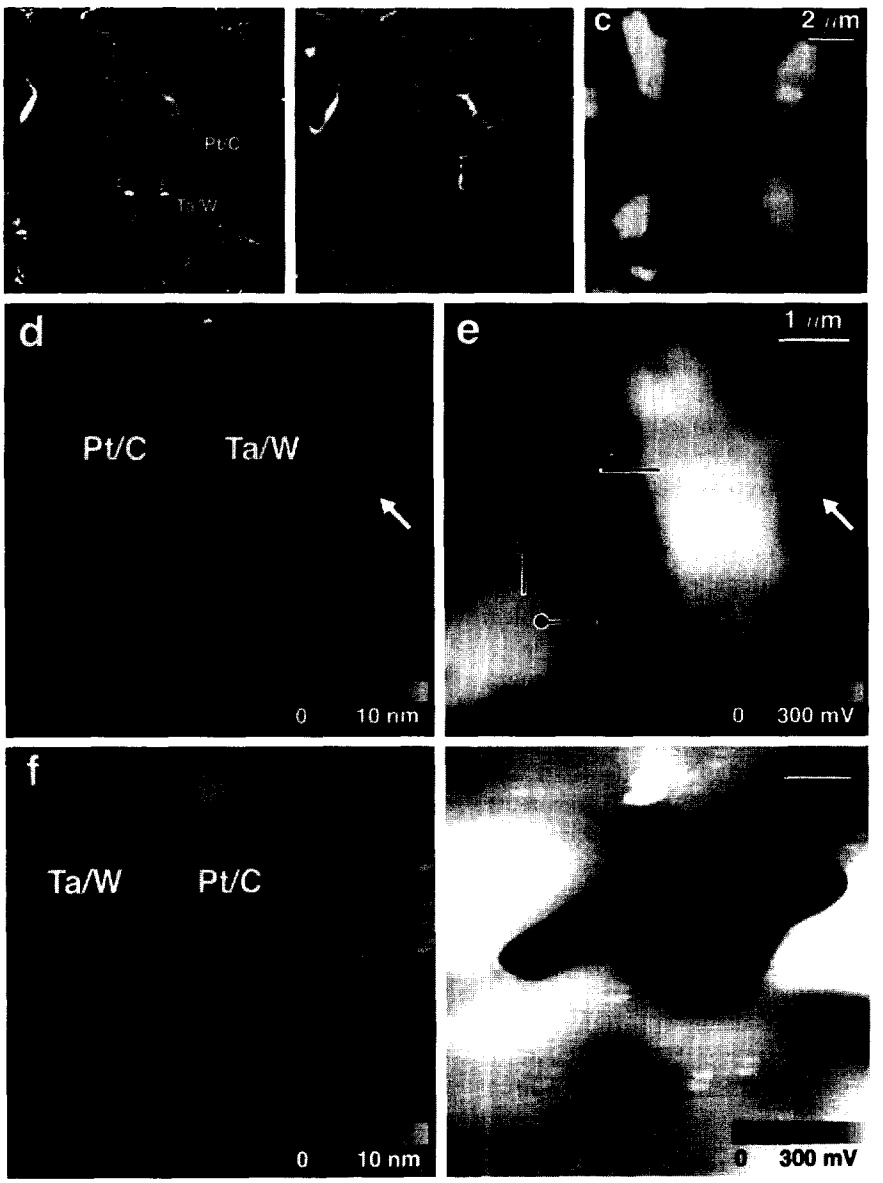

Fig. 6. Topography and surface potential of structured metal films. The top row shows a larger region of a structured Pt–C film on top of a Ta–W film. (a) Topography taken in tapping mode. (b) Backscattered electron image of the same region taken in an SEM (Hitachi S-900) confirming that the two layers are truly comprised of different materials. The black arrow points to a third material patch explained in the text. (c) Measured surface potential. (d) and (e) Close-up of topography and surface potential of area marked in (a). The black arrows point to the additional patch of a third material marked in (b). Surface features down to ~ 80 nm can be seen in the potential image (white arrow). (f) and (g) Topography and surface potential of a structured Ta–W film on top of a Pt–C film (the obvious presence of a double-tip and strong-tip artifacts has no effect on the conclusions made). The dependence of tip–sample separation (Fig. 7) was studied along the three lines indicated in image (e). All potential images were taken at 15 nm lift height.

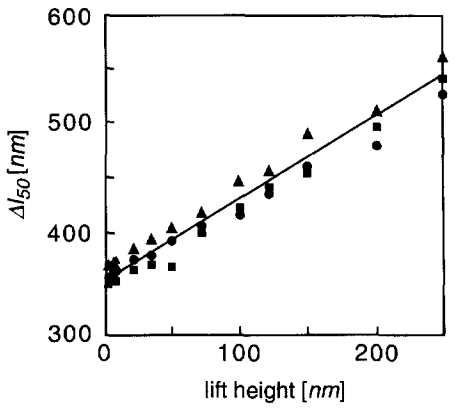

Fig. 7. Distance between 25% and 75% of the total measured voltage change Δl_{50} as a function of the lift height. Measurements were made along the three lines indicated in Fig. 6e.

negative after capturing an electron. This creates a theoretical potential difference of ~ 200 mV ($W_{\mathrm{vac,n\text{-}GaAs}} \approx 4.7$ eV and $W_{\mathrm{vac,p\text{-}GaAs}} \approx 4.9$ eV [19]) between the two regions. Furthermore, the material contrast between the $Al_{0.15}Ga_{0.85}As$ and AlAs layers could be measured as a small potential modulation of approximately 10 mV, which is only 10% of the theoretical value of ~ 100 mV ($W_{\mathrm{vac,AlAs}} \approx 4.7$ eV and $W_{\mathrm{vac,Al_{0.15}Ga_{0.85}As}} \approx 4.6$ eV [21]). As expected from our theoretical considerations, the small thickness of the layers causes an averaging over neighboring potentials. We can clearly attribute this modulation to the potential difference between the layers, because the oscillation amplitude of the cantilever during the lift cycle is substantially smaller than the lift height.

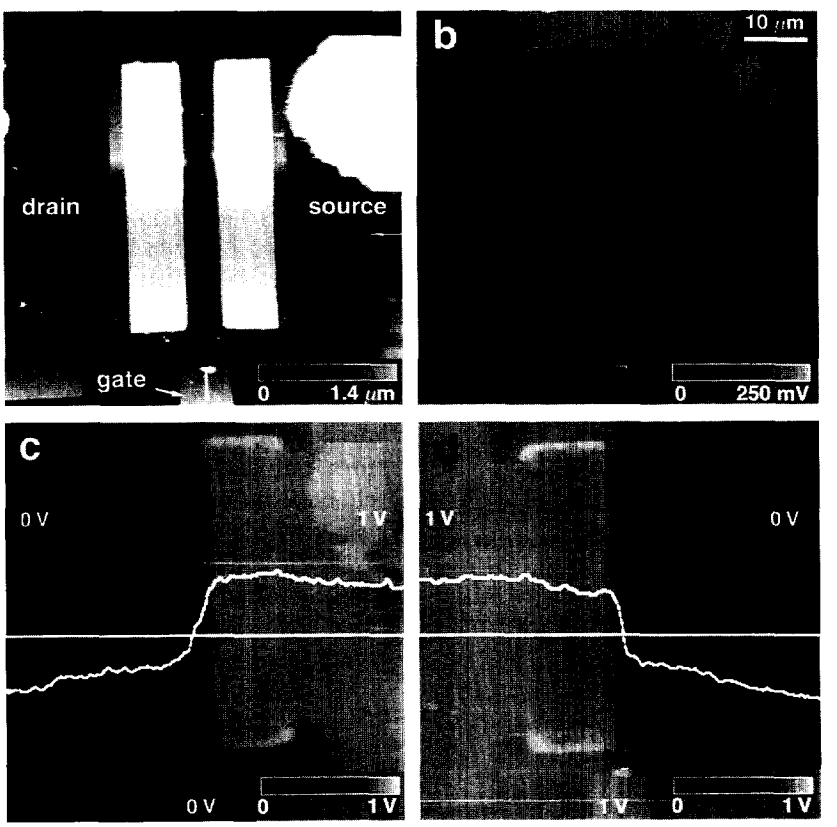

Fig. 8. Topography and surface potential on a GaAs-FET. (a) Topography, (b) surface potential without external voltage, (c) surface potential at $U_{ds} = U_{gs} = -1$ V, and (d) surface potential at $U_{ds} = U_{gs} = 1$ V. The potential images were taken at 15 nm lift height.

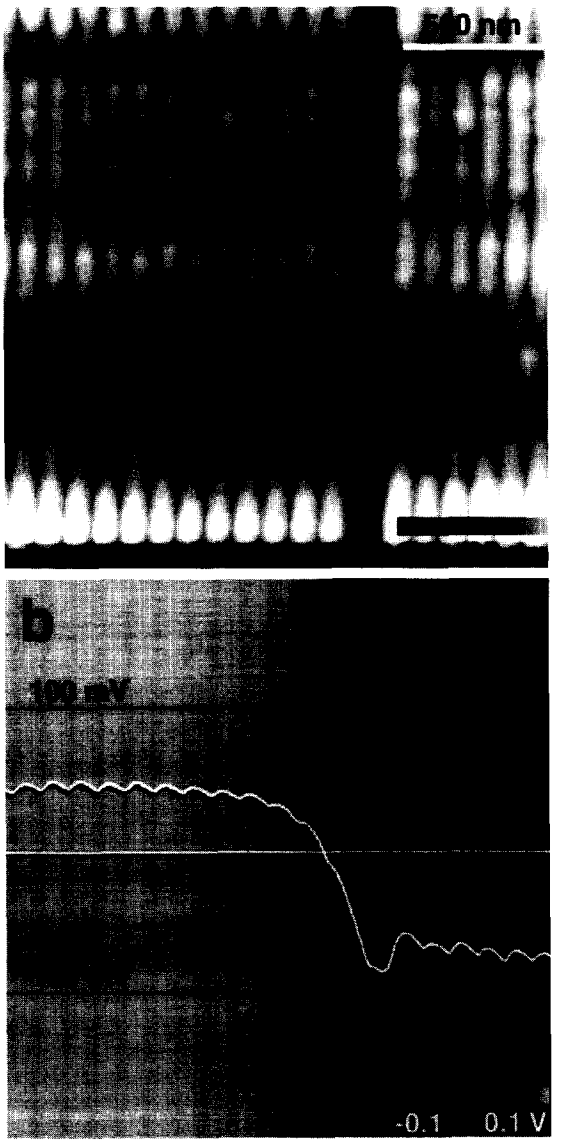

Fig. 9. Topography (a) and surface potential (b) of the cleaved surface of a vertical cavity laser (lift height 10 nm). The p–n junction is only visible in the potential image (n-doped region, left; p-doped region, right). Because of the stronger oxidation of the AlAs layers, the layered structure can be seen in the topography as well as in the potential image.

6. Discussion

In most of the previously published setups [8–13], topography and surface potential are measured using a cantilever excited by a piezo at its resonance frequency (ω_0) and, additionally, applying an AC voltage at a second frequency (ω_1) to the cantilever. Topography and surface potential are detected simultaneously by locking to the two frequencies ω_0 and ω_1, respectively. With this method, the measured topography is influenced by the other two long-range electrostatic force contributions (Eqs. (3) and (5)) which can overcome the short-range Van der Waals force because the AC voltage (usually between 5 and 10 Vpp) is always turned on [12]. The lift-mode technique overcomes this problem as no external voltage is applied to the probe when topography is imaged in tapping mode.

In all cases where we measured contact potentials, the measured contrast was smaller than expected. In the case of the Ta–W/Pt–C films, for example, the contact potential should be 1.3 V, based on the difference of the work functions ($W_{vac,Ta-W} \approx 4.3$ eV, $W_{vac,Pt-C} \approx 5.6$ eV [18]). However, the measured potential difference, 300 ± 20 mV (Fig. 6c, Fig. 6e, and Fig. 6g), is smaller than the above theoretical value. This general behavior is due to the fact that, for all structures, the measured potential contrast is an averaged value over all potential regions, where the ones just underneath the tip give the largest contribution. This also explains why the accuracy of the measured potentials decreases from larger to smaller structures, i.e. from the FET to the vertical cavity laser. Additionally, the contact potential difference depends on the condition of the surface, i.e. contamination, stress, temperature, crystalline structure, oxide-layer properties, or (trapped) charges [10]. For insulators care has to be taken to avoid transfer of charges during the topography tracing cycle (e.g. using true non-contact instead of tapping mode). Nevertheless, for the samples tested so far, we always obtained the expected sign and were able to distinguish between the different materials.

7. Conclusions

Surface potential microscopy using the Kelvin probe in lift mode offers a method to distinguish materials based on their electronic, i.e. chemical

properties without cross talk from topography. Whereas true electric potential information can only be gained from surface areas with dimensions very large compared to the probe, different materials can still be detected down to a few tens of nanometers in size, albeit with reduced contrast. Contrast and detection limit may be further improved, by employing longer and narrower probing tips.

Acknowledgements

The authors would like to thank M. Gnos, ETH Zurich, for providing the MMP simulation program and sharing his expertise with its use. The GaAs-FETs were kindly provided by Dr. W. Patrick, ETH Zurich. Dr. M. Moser, Paul Scherrer Institute, Zurich, generously provided us with a range of epitaxially grown heterostructures. Financial support from ETH Zurich and the Swiss National Science Foundation, Grant 4036-044062, is gratefully acknowledged.

References

[1] P. Muralt, D.W. Pohl, Appl. Phys. Lett. 48 (1986) 514.
[2] P. Muralt, H. Meier, D.W. Pohl, H. Salemink, Appl. Phys. Lett. 50 (1987) 1352.
[3] J.R. Kirtley, S. Washburn, M.J. Brady, Phys. Rev. Lett. 60 (1988) 1546.
[4] J.P. Pelz, R.H. Koch, Rev. Sci. Instr. 60 (1989) 301.
[5] S. Morita, Y. Maita, Y. Takahashi, Jpn. J. Appl. Phys. 28 (1989) L2034.
[6] Y. Martin, H.K. Wickramashinghe, Appl. Phys. Lett. 50 (1987) 1455.
[7] Y. Martin, D.W. Abraham, H.K. Wickramashinghe, Appl. Phys. Lett. 52 (1988) 1103.
[8] J.M.R. Weaver, D.W. Abraham, J. Vac. Sci. Technol. B 9 (1991) 1561.
[9] M. Nonnenmacher, M.P. O'Boyle, H.K. Wickramasinghe, Appl. Phys. Lett. 58 (1991) 2921.
[10] M. Nonnenmacher, M.P. O'Boyle, H.K. Wickramasinghe, Ultramicroscopy 42–44 (1992) 268.
[11] A. Kikukawa, S. Hosaka, R. Imura, Appl. Phys. Lett. 66 (1995) 3510.
[12] M. Yasutake, Jpn. J. Appl. Phys. 34 (1995) 3403.
[13] A. Kikukawa, S. Hosaka, R. Imura, Rev. Sci. Instr. 67 (1996) 1463.
[14] L. Novotny, D.W. Pohl, P. Regli, J. Opt. Soc. Amer. A 11 (1994) 1768.
[15] M. Gnos, P. Leuchtmann, Annu. Rev. Progress Appl. Comput. Electromagnet. 1 (1995) 81.
[16] T. Hartmann, R. Gatz, W. Wiegräbe, A. Kramer, A. Hillebrand, K. Liberman, W. Baumeister, R. Guckenberger, in: D.W. Pohl, D. Courjon (Eds.), Near Field Optics, Kluwer, Dordrecht, 1993, p. 35.
[17] M. Hegner, P. Wagner, G. Semenza, Surf. Sci. 291 (1993) 39.
[18] D. Lide (Ed.), Handbook of Chemistry and Physics, 74th ed., CRC Press, Boca Raton, 1993, pp. 12–105.
[19] S.M. Sze, Physics of Semiconductor Devices, Wiley, New York, 1981.
[20] F. Reinhardt, B. Dwir, G. Biasol, E. Kapon, Appl. Surf. Sci., in press.
[21] S. Adachi, J. Appl. Phys. 58 (1985) R1.